ARTICLE

Momentum-transfer model of valence-band photoelectron diffraction

G. Schönhense [1✉], K. Medjanik[1], S. Babenkov[1], D. Vasilyev[1], M. Ellguth[1,3], O. Fedchenko[1], S. Chernov[1], B. Schönhense[2] & H.-J. Elmers[1]

Recent instrumental progress of valence-band photoemission in the X-ray range allows uncovering bulk- and surface-related electronic properties. Four-dimensional recording of energy and momentum-vector gives access to the complete spectral-density function. Systematic measurements for a number of transition metals between 15 eV-6 keV reveal unexpected strong intensity modulations due to photoelectron diffraction. Here, we present a graphical model that illustrates the role of momentum-conservation in Fermi's Golden-Rule in an intuitive way. Intensity enhancement or reduction by factors >5 are confined to small energy- and momentum-intervals (widths $0.03\,\text{Å}^{-1}$ and $200\,\text{meV}$). Laue-type diffraction involves the photon momentum and is intrinsic in the photoemission process, in accordance with Pendry's final-state-model. At higher energies, Kikuchi-diffraction imprints additional modulations on valence-band-patterns and quasi-elastic background. The absence of photon-momentum transfer uncovers the extrinsic nature of Kikuchi-diffraction. For Re at 30 K and 3.4 keV the relative weight of the Kikuchi-branch is comparable to the Laue-branch, whereas at 6 keV the Kikuchi-branch prevails.

[1] Institut für Physik, Johannes Gutenberg-Universität, Staudinger Weg 7, 55128 Mainz, Germany. [2] Department of Bioengineering, Imperial College, South Kensington Campus, London SW7 2AZ, UK. [3] Present address: Surface Concept GmbH, Am Sägewerk 23a, 55124 Mainz, Germany. ✉email: schoenhe@uni-mainz.de

Thanks to the increased probing depth, angular-resolved photoelectron spectroscopy (ARPES) in the X-ray range is rapidly gaining importance in solid-state physics and materials research. Access to the true bulk electronic structure is an important achievement, e.g. for a detailed study of correlated and quantum materials. The potential of soft-X-ray ARPES is demonstrated in refs. [1,2], a comprehensive overview of hard X-ray photoelectron spectroscopy (HAXPES) is given in ref. [3].

The wavelength of the excited photoelectron is smaller than the interatomic distances, giving rise to X-ray photoelectron diffraction (XPD). Core-level XPD (CL-XPD) is a powerful method probing the geometrical structure of the photo-emitting atomic layers, surface reconstruction and relaxation, as well as adsorbate sites and distances (see excellent overviews[4–12]). In early work angular-distributions were interpreted as being caused by photoelectron-reflection on lattice planes of the crystal[13–15]. A two-beam dynamical theory was applied to explain the azimuthal variations of intensities[16,17]. XPD cluster-models showed fair agreement for clusters down to few nm[18]; at higher energies a Bloch-wave approach to XPD has proven more appropriate[8].

CL-XPD is well understood, but thus far, data for valence-band XPD (VB-XPD) are sparse (e.g refs. [19–23]) due to the complexity of the process. The roles of band dispersion, initial electron momentum and photon momentum in VB-XPD is not a priori clear. Early studies in the high-energy, high-temperature, low k-resolution limit revealed matrix-element weighted densities of states (MEWDOS), modulated by XPD effects[19,21]. The results could be interpreted analogously to CL-XPD after integrating over an energy range of a few eV[23] or by the assumption of a localization of the band electrons[19] as explained in orthogonalized-plane-wave approximation[24]. It was found that the initial-state orbital angular momenta influence the VB-XPD signal[22]. One-step photoemission theory made impressive progress at high energies[25] and today is close to the stage of predicting VB-XPD features as shown in this article.

VB k-patterns in the hard X-ray range show a strong background from thermal-diffuse scattering, which is modulated by Kikuchi-type diffraction[26]. Its intensity depends on temperature and mass number of the relevant atom species and increases strongly with increasing energy and temperature, as described by the Debye−Waller Factor. The same Kikuchi patterns are measured as CL-XPD at identical kinetic energy and k-field of view and can be used for a strong reduction of the modulated background. However, after this correction, regions of significant local intensity enhancements remain.

In the present work, we discuss the different classes of Laue- and Kikuchi-type VB-XPD and present a graphical model for quantitative analysis. The work was motivated by the appearance of strong local intensity modulations in valence-band mapping of various transition metals. Figure 1 shows an overview for the d-bands of Mo(110), W(110), Re(0001) and Ir(111) in a polar angular range of 0–8° at an angular resolution <0.03°. All examples exhibit pronounced local intensity enhancements up to a factor of 5 (marked by dashed ellipses) in small regions of the momentum-energy parameter space (Δk-regions down to 0.03 Å^{-1}; ΔE_B down to 200 meV), overlaid on the valence-band patterns. The intensity distributions look irregular and do not reflect the crystal symmetry. Some patterns reveal regions where the band-features appear attenuated (arrows), pointing on destructive interference. If disregarded, this substantial influence of photoelectron diffraction on the observed band-features including their dichroism and spin-polarization can cause misinterpretations with respect to the spectral function and its spin-character.

Results

Momentum-space description of valence-band photoemission. Within first-order time-dependent perturbation theory, the photoemission intensity can be derived from Fermi's Golden Rule describing the transition probability W from an initial state φ_i to a final state φ_f,

$$W = \frac{2\pi}{\hbar}|<\varphi_f|\Delta|\varphi_i>|^2\delta(E_f - E_i - h\nu), \qquad (1)$$

where the perturbation operator Δ represents the electromagnetic field including its polarization state[27,28]. The δ-function accounts for energy conservation. Momentum-conservation is discussed below using a graphical intuitive model instead of a second δ-function.

X-ray photoemission is described by direct transitions into quasi-free-electron-like final states with parabolic dispersion of the final-state energy E_{final} versus final-state momentum k_f, but with an effective mass m_{eff} that can still differ from the free-electron m_e

$$|\mathbf{k}_{final}|/\text{Å}^{-1} = (1/\hbar)\sqrt{(2m_{eff}E_{final})} = 0.512\sqrt{(m_{eff}/m_e)}\sqrt{(E_{final}/\text{eV})};$$
$$E_{final} = h\nu - E_B + V_0^*. \qquad (2)$$

There is no "universal" final-state parabola that is valid throughout a large energy range. Rather, the final-state effective mass m_{eff} and V_0^* (here referred to E_F) are empirical fit parameters. For tungsten, $m_{eff}/m_e = 1.07$ at 1 keV[29] and 1 at 6 keV[30]. For molybdenum, we found $m_{eff}/m_e = 1.035$ at 460 eV and 1 already at 1.7 keV. In general, m_{eff} could be (weakly) direction-dependent. However, we are not aware of any experimental indication of that in the X-ray range. The polarization-dependence in the operator in Eq. (1) causes the symmetry selection-rules[31]. The final state φ_f is described as multiple-scattering state (also termed "time-reversed LEED-state"; LEED: low-energy electron diffraction) as introduced by Pendry et al.[32–35].

Momentum microscopes observe a photo-transition directly in k-space, as illustrated in the k-space scheme (Fig. 2a, b) for Mo (110). In the periodic zone scheme, each Brillouin zone (BZ) contains the full set of valence bands. The spectral-density $\rho(E_B, \mathbf{k})$ can be considered as a multitude of surfaces in 3D k-space (one for each value of E_B). Different energies then give different 2D-cuts (which we term *energy isosurfaces*) through this volume, one of which is the Fermi surface. These isosurfaces are often fragmented into isolated electron and hole pockets and appear as periodically repeated patterns, identical in all BZs. This notion is different from the conventional description in terms of E-vs.-k plots for certain high-symmetry k-directions. Energy isosurfaces are a convenient basis describing XPD for itinerant initial states because the initial $\mathbf{k}$-vectors can easily be accounted for in the momentum-balance. The background patterns in Fig. 2a, b are cuts of the isosurfaces at E_F and $E_B = 1$ eV in the plane of photon incidence (here ΓNN-plane as indicated by the dashed line in Fig. 2c).

Photon-energy $h\nu$ and photon-momentum $\mathbf{k}_{h\nu}$ are both transferred to the photoelectron; energy- and momentum-balance have to be considered independent from each other. Energy conservation demands that all final states are located on a sphere with radius $|\mathbf{k}_f|$ given by Eq. (2). The (k_x, k_z)-schemes in Fig. 2a, b are to scale for the lattice constant of Mo. The transition at $h\nu = 400$ eV leads to the fourth repeated BZ. The 4D-character of the photoemission process is evident: the photon-energy dependence for a given binding energy (Fig. 2a, for E_F) and the binding-energy dependence for a given photon energy (Fig. 2b, for $h\nu = 400$ eV) both lead to sets of different final-state spheres.

Momentum conservation demands that the vector $\mathbf{k}_{h\nu}$ must be added to each final-state momentum vector $\mathbf{k}_f$. This is equivalent
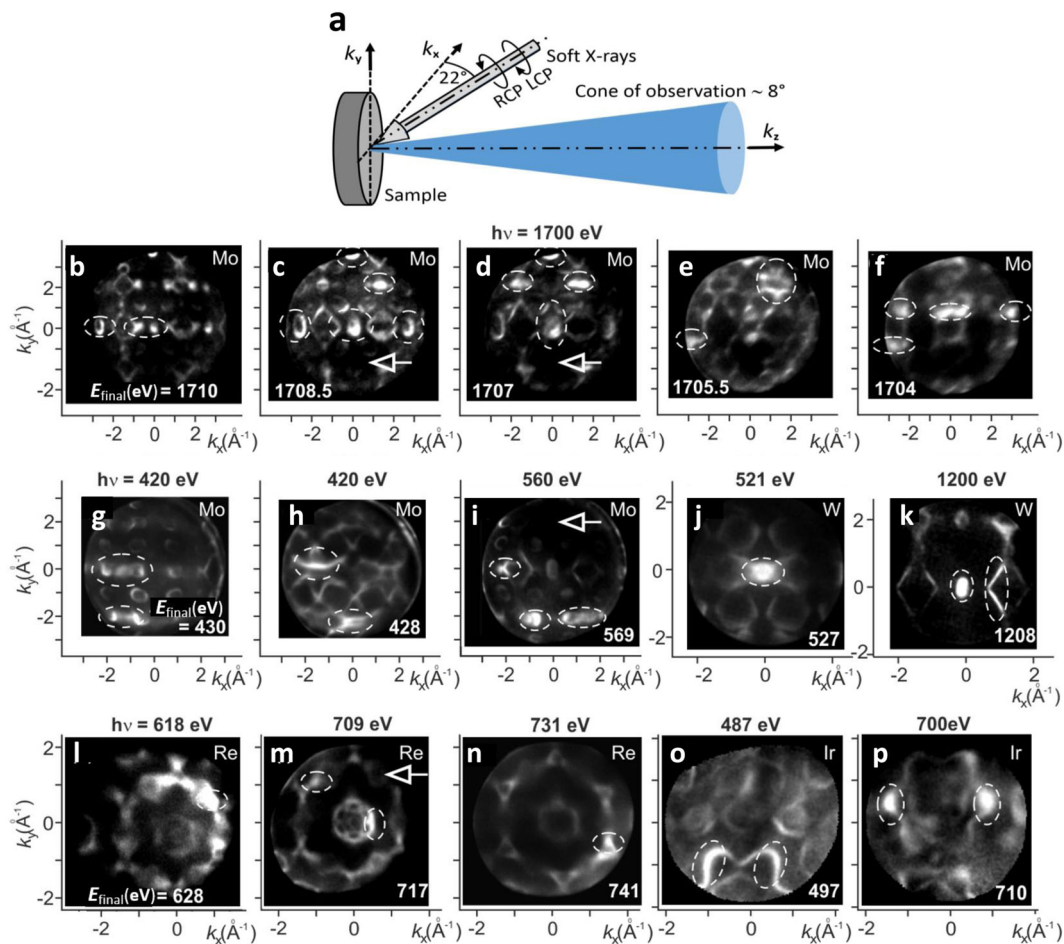
Fig. 1 Overview of valence-band photoelectron-diffraction patterns observed in *k*-microscopy. a Geometry of the experiment; k_x, k_y and k_z define the momentum coordinates, RCP and LCP denote righ- and left-circularly polarized light. **b**–**i** Momentum distributions taken for Mo(110), **j**, **k** for W(110), **l**–**n** for Re(0001), **o**, **p** for Ir(111). Photon energies and final-state energies E_{final} are denoted in the panels. Areas of local intensity enhancement are marked by dashed ellipses, local extinctions by arrows. Note the "irregular" patterns of local intensity modulations and the strong variations in (**b**–**f**), all taken at $h\nu = 1700$ eV but at five different kinetic energies, separated by increments of only 1.5 eV. The Debye−Waller factor was increased by cooling the samples to 40 K, energy resolution ~70 meV.

to a displacement of the centre *C* of the final-state sphere from the origin $k = (0,0,0)$ by $k_{h\nu}$. This shift of the sphere is directly visible in a *k*-microscope and can be quantified in the observed momentum patterns (see, e.g., Fig. 3 in ref. [29]). The shift of the sphere by $k_{h\nu}$ is relatively small at 400 eV but becomes substantial for hard X-rays.

Figure 2d–g shows 3D-views of four selected energy isosurfaces, the Fermi surface and those at $E_B = 1$, 2 and 3 eV. These surfaces have been determined experimentally as described in ref. [29]; see Methods section. Clearly, the shape of the isosurfaces changes rapidly with binding energy, which is just a full-3D-view of band-dispersion. Bands with negative curvature at E_F have hole-character like the N-pocket (growing with increasing E_B, compare (Fig. 2d, f)), positive curvature indicates electron-character like the octahedron centred at the Γ-point that shrinks with increasing binding energy. The background patterns in Fig. 2a, b are (k_x, k_z)-cuts through the isosurfaces (Fig. 2d, e). In general, $k_{h\nu}$ has an arbitrary direction with respect to the reciprocal lattice, and then schemes must consider full 3D *k*-space. The advantage of this representation is that it immediately shows all the initial *k*-vectors in a plane (Fig. 2a, b) or in 3D *k*-space (Fig. 2d–g) corresponding to a certain energy. This is an indispensable ingredient for the description of VB-XPD.

The umbrella-shaped caps of Fig. 2d–g mark the intersection areas of the given isosurface with the final-state sphere, here the NHP-plane. The band-structure pattern on the curved intersection area is observed by the momentum microscope. Thanks to the 3D-recording scheme of the ToF-microscope, all values of E_B in the energy-range of interest are recorded simultaneously. We note the analogy with the Ewald-sphere construction in electron diffraction: A diffraction spot occurs wherever the Ewald sphere intersects a reciprocal lattice point; a photoemission signal occurs wherever the final-state-sphere (displaced by $k_{h\nu}$) intersects a band feature in one of the repeated Brillouin zones.

The Ewald sphere does not give information on the intensity of diffraction spots or on systematic extinctions. Likewise, the intersection region of the final-state sphere with the periodic pattern of isosurfaces only shows where band features are visible in principle (obeying energy and momentum conservation). The actual photoemission intensity of a band depends on the matrix element in Eq. (1) that also accounts for the photon polarization (symmetry selection rules[31]).

The 1D case of Bragg-scattering at lattice planes parallel to the surface. The proposed model of VB-XPD describes transitions from itinerant band-states to final-state plane waves (wavevector k_f) extending over many unit cells, being diffracted at the lattice.
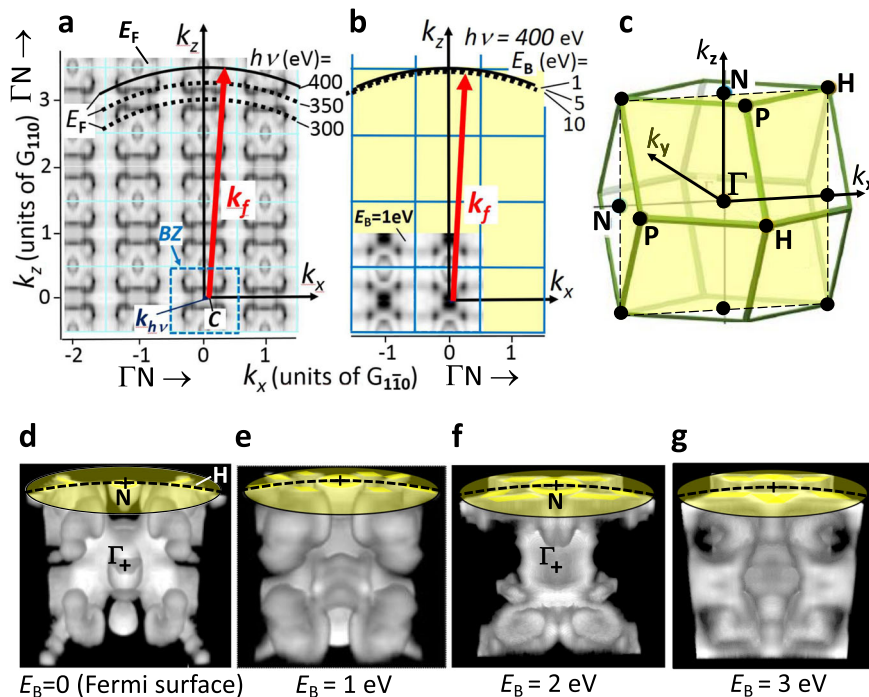
Fig. 2 Momentum-space description of a photo-transition from the valence band. a, b (k_x, k_z)-schemes describing direct interband transitions into a quasi-free-electron-like final state band at photon energies between 300 and 400 eV. The axes denote the momentum components k_x and k_z in units of the reciprocal lattice vectors G_{1-10} and G_{110}, respectively, both along the high-symmetry direction ΓN. The plots are to scale for the body-centred cubic metal Mo. The final-state momentum k_f (radius of the final-state sphere) depends on photon energy $h\nu$ (for fixed binding energy E_B) (**a**) and on E_B (for fixed $h\nu$) (**b**). The centre of the sphere C is displaced from the origin $\boldsymbol{k} = (0,0,0)$ by the vector of the photon momentum $\boldsymbol{k}_{h\nu}$. The background patterns are cuts (at $k_y = 0$)) of the periodically repeated measured spectral-density arrays for the Fermi energy E_F (**a**) and for $E_B = 1$ eV (**b**). Dashed square in (**a**) marks the first Brillouin zone (BZ), dark denotes high spectral density. **c** Brillouin zone of bcc lattice with high-symmetry points; plane ΓNN (yellow) is shown in (**a, b**). **d–g** Measured energy isosurfaces ($E_B =$ const. surfaces) at the Fermi energy (**d**) and at $E_B = 1$, 2 and 3 eV (**e–g**). The umbrella-shaped top marks the intersection area with the final-state sphere, which is recorded in a momentum microscope.

This is the concept of Pendry's model of the "multiple-scattering" photoemission final state[32–35]. In order to stay within the description of Fig. 2, we translate Bragg's law to k-space. For constructive interference in normal-emission, an integer-multiple of the photoelectron wavelength λ_e must coincide with the spacing d_z of the atom planes. In backward-scattering the path difference is twice the spacing d_z. With the reciprocal-lattice vector perpendicular to the surface $|\boldsymbol{G}_z| = 2\pi/d_z$ and the final-state electron momentum $|\boldsymbol{k}_f| = 2\pi/\lambda_e$, we obtain the corresponding relations in k-space:

$$d_z = n\lambda_e \quad \boldsymbol{k}_f = n\boldsymbol{G}_z \quad \text{forward} - \text{scattering}, \quad (3)$$

$$d_z = \frac{n}{2}\lambda_e \quad \boldsymbol{k}_f = \frac{n}{2}\boldsymbol{G}_z \quad \text{backward} - \text{scattering}. \quad (4)$$

Destructive interference occurs when the phase-shift difference is $\frac{2n-1}{2}\pi$, which can lead to an attenuation of band features as visible in Fig. 1 (arrows).

The graphical expression of Eqs. (3) and (4) is shown in Fig. 3a, b, respectively. For low photon energies ($\boldsymbol{k}_{h\nu}$ negligible), Eqs. (3) and (4) mean that the final-state-sphere intersects the centre (or the boundary) of a Brillouin-zone. At X-ray energies the shift of the final-state sphere by $\boldsymbol{k}_{h\nu}$ causes a deviation from this simple rule. For the experiments shown below, the angle of incidence is 68° from the surface normal; hence, the in-plane and perpendicular components of the shift are $|\boldsymbol{k}_{h\nu}| = 0.93|\boldsymbol{k}_{h\nu}|$ and $\boldsymbol{k}_{h\nu}^{\perp} = 0.37|\boldsymbol{k}_{h\nu}|$, the latter acting in negative k_z-direction. The k-microscope records the intensity pattern on a spherical section close to normal emission, sketched as yellow "cap" in Fig. 3a, b.

At a typical soft-X-ray energy (400 eV), we have $|\boldsymbol{k}_{h\nu}| = 0.20\,\text{Å}^{-1}$ and $\boldsymbol{k}_{h\nu}^{\perp} = 0.07\,\text{Å}^{-1}$ which is only 2.4% of the reciprocal lattice

vector $\boldsymbol{G}_z = \boldsymbol{G}_{110} = 2.824\,\text{Å}^{-1}$ for Mo(110). $|\boldsymbol{k}_{h\nu}|$increases linearly with $h\nu$, whereas $|\boldsymbol{k}_f| \sim h\nu^{1/2}$; hence, at 6 keV we find $|\boldsymbol{k}_{h\nu}| = 3.0\,\text{Å}^{-1}$. For Re(0001) $\boldsymbol{k}_{h\nu}^{\perp} = 1.1\,\text{Å}^{-1}$ is 79% of the reciprocal lattice vector $\boldsymbol{G}_z = \boldsymbol{G}_{0001} = 1.41\,\text{Å}^{-1}$, i.e. the displacement along k_z is almost a full BZ. The interference criterion is that the k-distance between the shifted centre of the sphere and the "cap" obeys the rules of Eqs. (3) or (4).

Valence-band XPD in 3D k-space. Forward scattering is the most easily explained component of VB-XPD. However, it only captures a small fraction of all possible scattering processes involving arbitrary reciprocal lattice vectors $\boldsymbol{G}$ of 3D momentum space. The generalization of Eqs. (3) and (4) in 3D k-space is the Laue equation:

$$\boldsymbol{k}_f = \boldsymbol{k}_f' - \boldsymbol{G}. \quad (5)$$

Momentum- and energy-balance demand the following five conditions: (i) the momentum of the electron in the initial itinerant state must be included, (ii) the photon momentum vector $\boldsymbol{k}_{h\nu}$ is transferred to the photoelectron, (iii) the diffraction process itself obeys the Laue equation (momentum transfer $\boldsymbol{G}$), (iv) the final-state energy E_{final} is preserved (all states lie on the same sphere, shifted by $\boldsymbol{k}_{h\nu}$), (v) the diffraction process leads to the same E_B-isosurface.

The k-space-model accounts for these conditions as follows: Energy isosurfaces like the experimentally determined ones in Fig. 2d–g give the complete initial $\boldsymbol{k}$-distribution (i), which strongly depends on binding energy. Condition (ii) is fulfilled by a rigid shift of the final-state sphere by $\boldsymbol{k}_{h\nu}$ with respect to $\boldsymbol{k} = (0,0,0)$. Final-energy-condition (iv) is fulfilled by plotting the
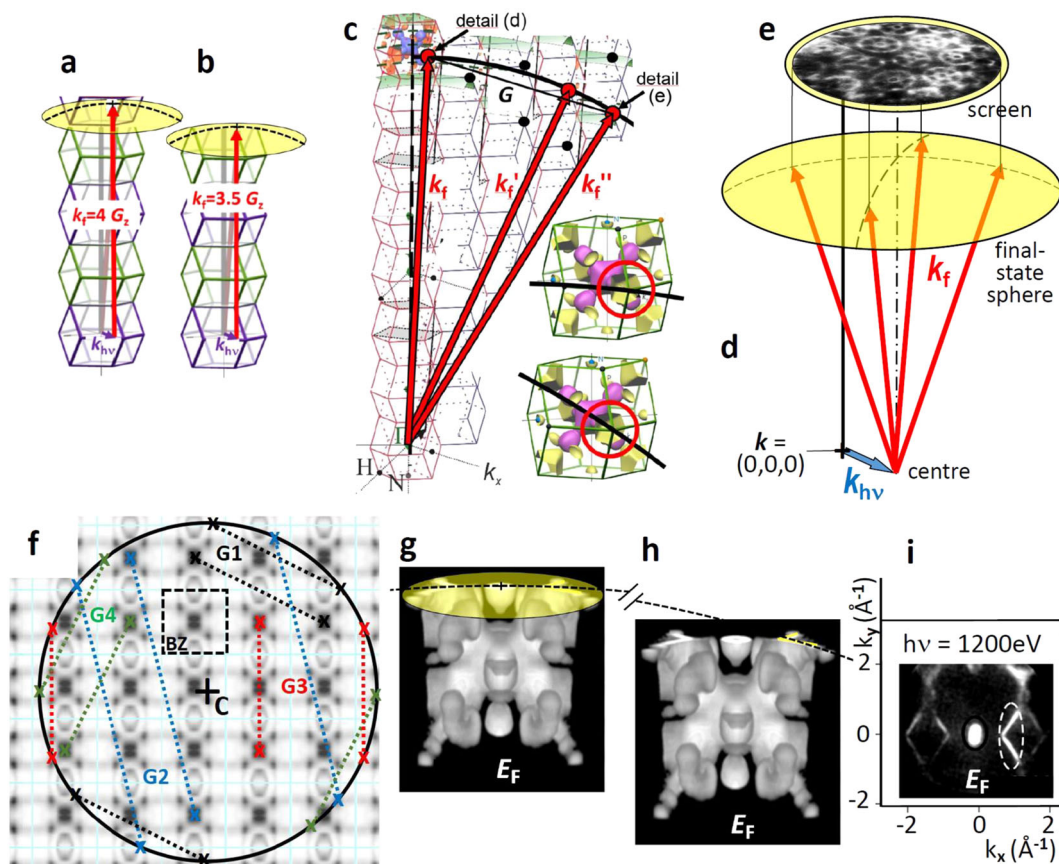
Fig. 3 Momentum-space model of photoelectron diffraction. a, b Direct transitions fulfilling conditions for constructive interference in normal emission due to forward (**a**) and backward-scattering (**b**). **c** The general case, resembling the Ewald construction, a graphical way to find "spots" where the Laue condition ($k_f' - k_f = G$) is fulfilled. **d** Details marking (E_B, k)-sectors, where the final-state sphere intersects identical regions in different repeated Brillouin zones. Vectors k_f, k_f' and k_f'' are located on the same final-state sphere and reach equivalent points. Reciprocal lattice vectors G give their distances. **e** Schematic 3D view showing the vector structure of the transition; length of vector $k_{h\nu}$ exaggerated for clarity. The spherical section is projected onto the planar screen. **f** Scheme illustrating that all reciprocal lattice vectors inside of the final-state sphere correspond to two specific (E_B, k)-sectors on the sphere, fulfilling the Laue equation. BZ marks the Brillouin zone, G1—G4 denote reciprocal lattice vectors. **g-i** Example of the mechanism described in (**c**), measured for Mo at E_F, $h\nu = 1200$ eV and k_z close to the border of the Brillouin zone (plane through the high-symmetry points NHP): the V-shaped band on the right-hand side of the field of view is cut by the final-state sphere in two different Brillouin zones (**g**) and (**h**), leading to a strong enhancement of the observed intensity (**i**).

photo-transition on a final-state-sphere with radius k_f (with the centre being shifted according to condition (ii)). Binding-energy condition (v) is fulfilled by plotting the isosurface with the correct E_B as periodic pattern in the extended zone scheme, like the two cases in Fig. 2a, b.

The remaining task is to fulfil condition (iii). It means that we search for intersection points of the final-state sphere for a given E_B with equivalent k-points in different repeated BZs, fulfilling the Laue equation. Such cases are illustrated in Fig. 3c, where the vectors k_f' and k_f'' reach the same band feature as vector k_f, but in different BZs. The red circles in insets of Fig. 3d mark the (E_B, k)-regions, where the final-state sphere intersects such identical points. Their distances are given by certain reciprocal lattice vectors G. In complete analogy to the Ewald construction, energy conservation demands that both ends of G must lie on the final-state sphere, which defines the (E_B, k)-region where the intensity is enhanced by VB-XPD. The scheme in Fig. 3e illustrates the 3D-nature of the momentum-transfer scenario. The planar detector-screen captures the projection of the curved cap.

All vectors G, which are completely inside of the final-state sphere, fulfil the diffraction condition on opposite sides of the circle (Fig. 3f) and at a multitude of positions on the sphere. Each of the dotted coloured lines **G1–G4** represent a certain reciprocal

lattice vector that is shifted such that it touches the sphere with both ends. Since G is a reciprocal lattice vector, its two ends touch identical points of the (reduced) BZ. Each G corresponds to a specific (E_B,k)-region on the shifted sphere where the Laue condition is fulfilled. If a band feature runs through such a region, its intensity is enhanced by VB-XPD.

Figure 3g–i shows an example for Mo at $h\nu = 1200$ eV, for the Fermi energy and a k_z-section through the NHP-plane of the BZ (Fig. 2c). The right V-shaped region on top of the isosurface is crossed by the final-state-sphere in two different BZs (Fig. 3g, h). In turn, the intensity of this feature in the measured momentum pattern is enhanced by VB-XPD (dashed ellipse in Fig. 3i). Here it becomes clear why the VB-XPD patterns look irregular and do not reflect the lattice symmetry: The shift of the final-state sphere by $k_{h\nu}$ breaks the symmetry. For example, in the case of Fig. 3f, the diffraction condition on the left and right side (red line $G3$) is fulfilled for different regions of BZ.

With respect to the "continuum" of kinetic energies the situation resembles Laue diffraction using a broad-band X-ray beam. However, the band dispersion poses additional constraints that—together with the broken symmetry—make the situation quite complex. "k-space movies" (Supplementary Videos 1–5) illustrate this puzzling behaviour. Most important
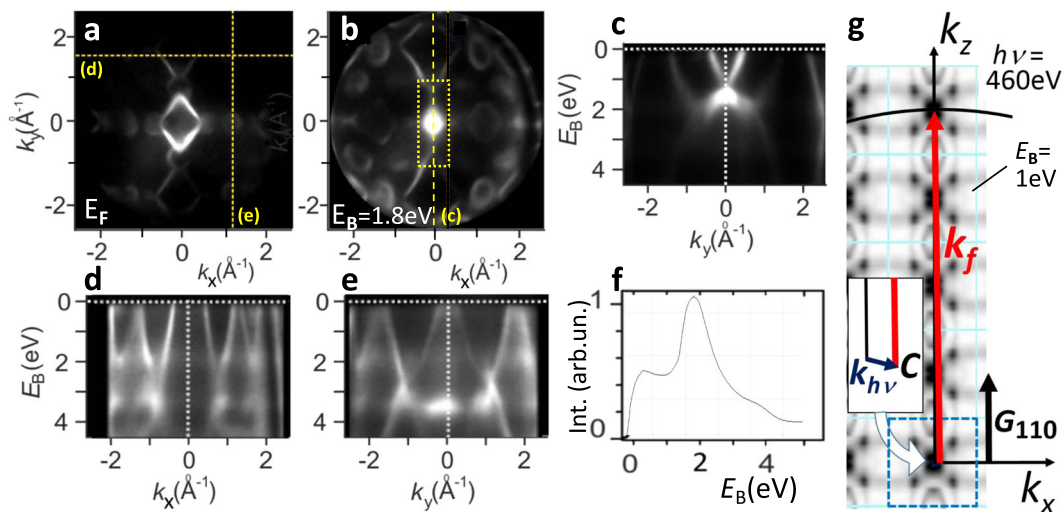
Fig. 4 Pronounced forward scattering in normal emission for valence-band photoelectrons from the Mo(110) surface at $h\nu = 460$ eV. a–c Tomographic-like $k_x - k_y$ momentum sections through the region of maximum intensity enhancement, visible in the isosurfaces at the Fermi energy (**a**), a binding energy of $E_B = 1.8$ eV (**b**) and in the $E_B - k_y$ section (**c**) along the dashed line in (**b**). **d**, **e** $E_B - k_x$ and $E_B - k_y$ sections in regions away from the interference condition, showing a much lower and more evenly distributed intensity; sections along the dashed lines in (**a**). **f** Integrated photoemission-intensity versus binding-energy taken from the dotted rectangle in (**b**), illustrating the intensity enhancement. **g** Scaled transition scheme for Mo(110) at 460 eV in the $k_z - k_x$ plane; the final-state sphere intersects the centre of the fourth repeated Brillouin zone (diffraction condition $\boldsymbol{k}_f = 4\boldsymbol{G}_z$).

are the different roles of the two relevant energies, E_{final} and E_B. The former defines the wavelength of the photoelectron, which governs diffraction dynamics. The latter defines the relevant isosurface of the spectral function $\rho(E_B, \boldsymbol{k})$ which is strongly energy dependent, giving rise to the strong diffraction modulation on the eV-scale (Fig. 1a–e). In CL-XPD E_B is fixed and there is no E-vs.-$\boldsymbol{k}$ dispersion; hence, only one energy- and one momentum-condition exist.

Experimental results for near-normal emission. Figure 4 shows a typical example for strong intensity enhancement around the centre of the $k_x - k_y$ distribution (Fig. 4a, b) with maximum intensity at $E_B \sim 1.8$ eV, also visible in the $E_B - k_y$ section (Fig. 4c). In comparison, $E_B - k_x$ and $E_B - k_y$ sections away from normal emission show a much lower intensity and more homogeneous intensity distributions along the bands (Fig. 4d, e). Figure 4f reveals the spectral dependence of the intensity-enhancement, integrated over the rectangular area marked in Fig. 4b. The diffuse background shows horizontal "stripes" of enhanced intensity in Fig. 4d, e, which are a fingerprint of quasi-elastic thermal-diffuse scattering. Their energy position (here ~1.8 and 3.3 eV) corresponds to maxima in the matrix-element weighted density of states (MEWDOS) as discussed in refs. [19,21,23,30]. The MEWDOS stripes appear inhomogeneous, which might point on a directional dependence of the diffuse scattering effect.

We analyse the transition by the quantitative scheme in Fig. 4g, with $G_z = G_{hkl} = G_{110} = 2.824$ Å^{-1} and $k_{h\nu} = 0.23$ Å^{-1} ($k_{h\nu}^{\perp} = 0.09$ Å^{-1}; $|k_{h\nu}| = 0.21$ Å^{-1}). The intensity enhancement confirms Eq. (3) with $\boldsymbol{k}_f = 4\boldsymbol{G}_{110}$, shifted by the small value of $k_{h\nu}^{\perp}$ away from the Γ-point of the fourth repeated BZ. Such measurements provide a metric in k-space for the determination of the centres and boundaries of repeated BZs and for the empirical quantities m_{eff} and V_0^* in Eq. (2). Precise measurement of the energies of diffraction enhancement for two high-symmetry planes can yield both parameters. From the single measurement of Fig. 4, we derive $m_{eff} = 1.03\, m_e$ (1.04 m_e) assuming $V_0^* = 10$ eV (6 eV). Here the resulting m_{eff} depends only weakly on the assumed value of V_0^*.

This type of intensity enhancement occurs even in the VUV-range; see example for Re in Fig. 5. An intense spot of constructive interference appears in the centre of the $k_x - k_y$ images (Fig. 5a–c). The E_B-vs.-k_x sections (Fig. 5d–f) reveal that the enhancement is restricted to a small energy range of ~200 meV width. When varying the photon energy, this spot shifts in binding energy by the same amount, as revealed by the intensity profiles (Fig. 5g–i). Clearly, the constructive interference stays at fixed E_{final}, because this energy is relevant for the diffraction dynamics. The change of the enhancement from band to band excludes a matrix element effect. In the vicinity of E_F there is a total bandgap at the Γ-point, so we cannot follow the trend up to the Fermi energy. Given the lattice constants of Re and $k_{h\nu} \approx 0$, the centre of the second BZ is at $k_z = 2G_{0001} = 2.82$ Å^{-1} which agrees approximately with the given final state momentum. However, the final state is no longer free-electron-like, deviations from parabolic dispersion can occur and flat unoccupied d-bands can serve as additional final states.

Experimental results of VB-XPD for arbitrary reciprocal lattice vectors. The—at first sight puzzling—multitude of irregularly distributed regions of strong intensity enhancement observed for all materials studied so far (overview in Fig. 1) reflects the general case of Fig. 3c–i. Figure 6 shows an analysis for Mo(110) at $h\nu = 1700$ eV. With $k_f = 21.17$ Å^{-1} this transition leads to the eighth repeated BZ; $k_{h\nu} = 0.86$ Å^{-1} shifts the sphere by 45% of the BZ radius. The diameter of the k-field of view in Fig. 6a is ~6 Å^{-1}; hence, the first and four next BZs are visible. The $k_x - k_y$ and $E_B - k_x$ cuts (Fig. 6a, b) show pronounced intensity enhancement in a small region within 200 meV from the Fermi energy, whereas no enhancement is visible in the $E_B - k_y$ cut (Fig. 6c). Quantitative analysis by the transition scheme (Fig. 6d) reveals that the sphere crosses the identical feature for $\boldsymbol{k}_f' - \boldsymbol{k}_f = \boldsymbol{G}_{-1\,1\,0}$ (see details in Fig. 6e) and $\boldsymbol{k}_f'' - \boldsymbol{k}_f = \boldsymbol{G}_{-2\,14\,0}$. Both constructive interference conditions lead to the observed intensity enhancement (dashed ellipses in Fig. 6a, b).

In the terminology of a diffraction experiment, the low- and high-index cases $\boldsymbol{G}_{-1\,1\,0}$ and $\boldsymbol{G}_{-2\,14\,0}$ belong to the zero-order and a higher-order Laue-zone, respectively. Due to the forward
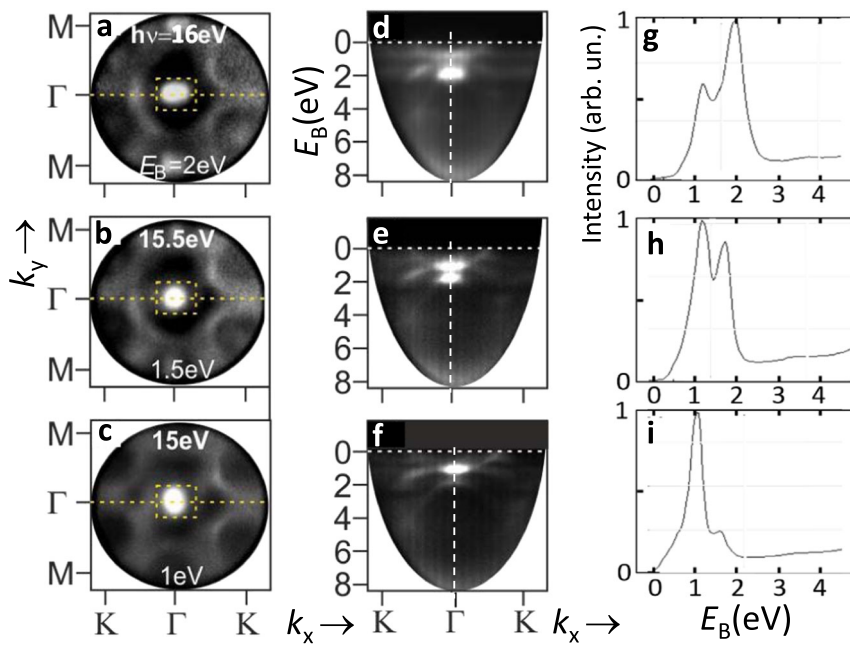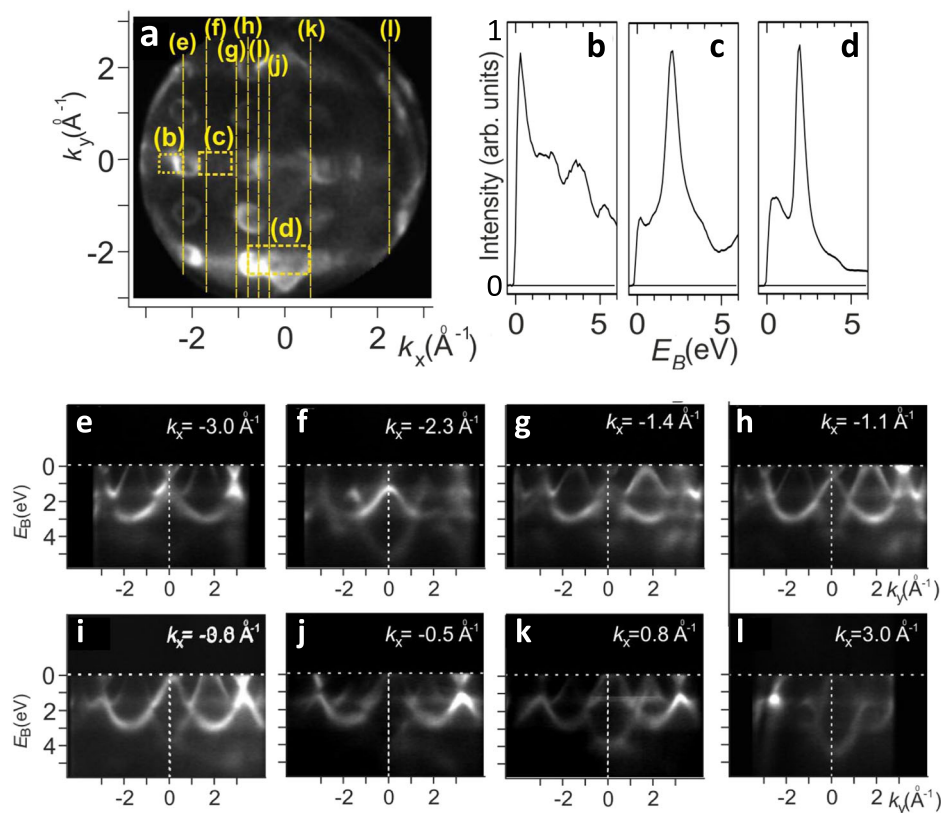
Fig. 5 Photon-energy dependence of valence-band photoelectron diffraction for Re(0001) between $h\nu = 15$ and 16 eV. a–c Momentum distributions in the $k_x - k_y$ plane; **d–f** corresponding sections of binding energy E_B vs. momentum component k_x along the dashed lines in (**a–c**). **g–i** Binding-energy profiles of the intensities in the areas marked by rectangles in (**a–c**). The interference condition shifts with photon energy; steps of 0.5 eV correspond to momentum steps of only 0.04 Å^{-1} along k_z.
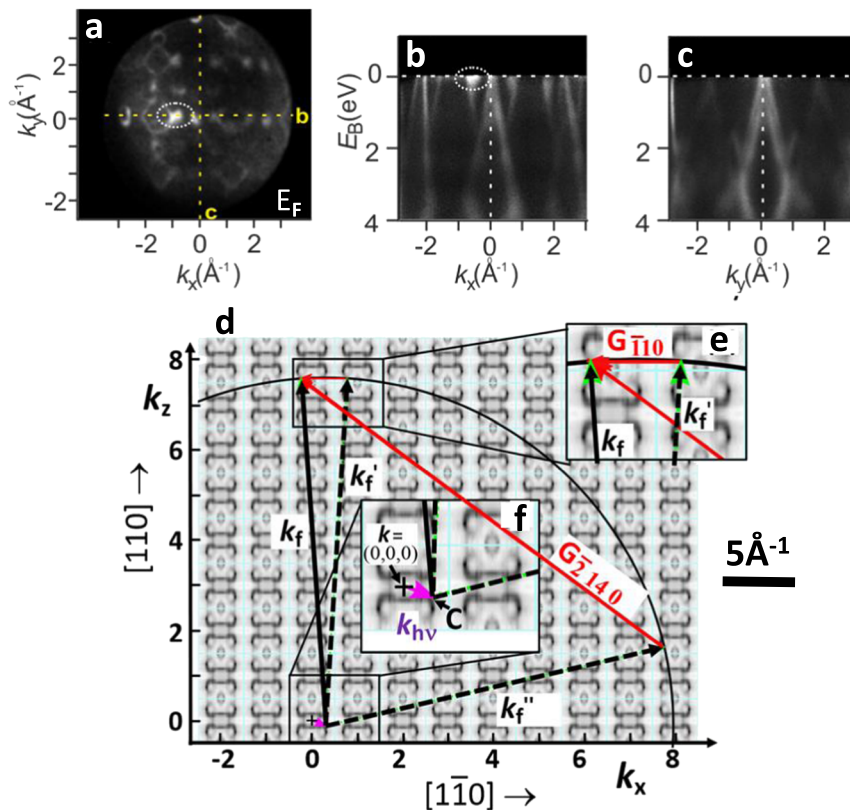
Fig. 6 Analysis of valence-band photoelectron diffraction for the Mo(110) surface at $h\nu = 1700$ eV. a Momentum distribution in the k_x-k_y momentum plane showing an intensity enhancement in a small local region (dashed ellipse). **b** Section of binding energy E_B vs. momentum component k_x along the dashed line in (**a**) revealing the energetic localization close to the Fermi energy E_F. **c** E_B vs. k_y section showing that there is no intensity enhancement in this plane. **d** Quantitative analysis yielding that the final-state sphere runs through the eight repeated Brillouin zone along k_z and crosses the identical feature for the Laue conditions $\boldsymbol{k}_f' - \boldsymbol{k}_f = \boldsymbol{G}_{-1\,1\,0}$ (details in (**e**)) and $\boldsymbol{k}_f'' - \boldsymbol{k}_f = \boldsymbol{G}_{-2\,14\,0}$. Vectors $\boldsymbol{G}$ are labelled by the Miller indices; the high index of 14 results from our choice of the k_x- and k_y-axes along crystallographic directions [110] and [1 –1 0]. The photon momentum $\boldsymbol{k}_{h\nu}$ causes a strong shift of the centre C of the sphere (details in (**f**)). The background pattern is the periodically repeated measured 4D array, cut at E_F and $k_y = 0$ (dark is high spectral density). Full data array for 1700 eV; see Supplementary Videos 1 and 2.

Fig. 7 Energy- and momentum-dependence of valence-band photoelectron diffraction for Mo(110) at a photon energy of 400 eV. a (k_x-k_y) momentum section at the Fermi energy E_F. **b–d** Intensity profiles revealing resonance-like intensity enhancements in the areas marked by rectangles in (**a**). **e–l** Binding energy E_B vs. momentum k_y sections at eight values of momentum k_x between -3 Å^{-1} and $+3$ Å^{-1} (along the dashed lines in (**a**)), revealing the variation of local intensity enhancements with energy and momentum. Although the photon momentum is rather small at 400 eV, the shift of the final-state sphere is sufficient to cause a striking left–right asymmetry in the patterns. Full data arrays of 400, 420 and 440 eV; see Supplementary Videos 3–5.

characteristic of scattering at keV energies, the diffracted intensity is larger for the smaller scattering angle, i.e. the lower Miller index. Note that here we consider only a planar cut through one quadrant. There will be many more such conditions when the full final-state sphere in 3D k-space is considered.

The sequence for Mo at $h\nu = 400$ eV in Fig. 7 captures some snapshots. The way how the positions for constructive interference "travel" through (E_B, k)-space is best visible in Supplementary Videos 3–5. The cut at E_F (Fig. 7a) and the intensity profiles (Fig. 7b–d), taken in the rectangular areas marked in Fig. 7a, reveal a number of regions with locally enhanced intensities. Electron- and hole-pockets appear as oval features (Fig. 7a) with inward or outward dispersion; see cuts in Fig. 7e–l, taken along the dashed lines in Fig. 7a. Enhanced intensities appear mostly in the second BZ at negative k_x and k_y values and show almost "resonance-like" VB-XPD enhancements.

Proving that the interference stays fixed on the E_{final}-scale like in Fig. 5 would require prohibitively long acquisition sequences in 0.5 eV photon-energy steps. In Figs. 4 and 6, high intensity in comparison with neighbouring bands and sudden intensity jumps along a band are used as criterion for VB-XPD. The enhancement in the electron ball (Fig. 7e) at the lower left rim of Fig. 7a shows a rather sharp cutoff at a binding energy of ~2 eV. Figure 7f shows the enhanced maximum of a band that stays well below E_F. Sequence Fig. 7g–j shows how the interference condition crosses the equivalent k-space object in the BZ at the bottom of Fig. 7a. The enhancement exhibits a characteristic "fine structure". Figure 7k extends the analysis to the other side of the bottom BZ and finally Fig. 7l returns to the object of Fig. 7e, but at opposite k_x and k_y. The small spot in Fig. 7l appears an order of

magnitude brighter as the surrounding bands. The horizontal stripes with enhanced brightness in Fig. 7a confirm the 3D-generalization of the graphical model in Fig. 3. For instance, in 3D the reciprocal lattice vector **G3** responsible for the red lines in Fig. 3f yields a full cylinder touching the final-state sphere along two rings.

Coexistence of Laue- and Kikuchi-type VB-XPD in the hard X-ray range. At hard X-ray energies, a new type of diffraction signature appears; experiments were performed at beamline P22 of PETRA III. Results for Re at $E_{final} = 3.4$ and 6 keV (Fig. 8) reveal that a significant background is superimposed on the as-measured valence-band k-distributions. This background is higher than for Mo at 1.7 keV (Fig. 6a). At 3.4 keV (Fig. 8a–h) valence-bands are visible as circles, originating from an electron-like tube centred at the A-point, and ellipses from elongated hole-pockets at the M-points. A lattice model is shown in Fig. 8i and the BZ with its high-symmetry points are defined in Fig. 8j. At $E_{final} = 6$ keV (Fig. 8k–m) the background is even higher, the VB-pattern looks irregular and band-structure features are hardly discernible. The most eye-catching features are pronounced dark spots (marked by crosses), two bright regions at the upper left rim (dashed ellipses) and a bright X-shaped feature (centre marked by a circled cross). Here the field-of-view (~12 Å^{-1}) comprises 19 BZs: the central one, and two rings with 6 and 12 BZs centred around it. On this large momentum scale, we observe something new. The as-measured VB-patterns (Fig. 8a, k) are modulated by pronounced long-range structures.

The key of understanding the long-range modulations lies in the comparison of as-measured VB k-patterns with CL-XPD
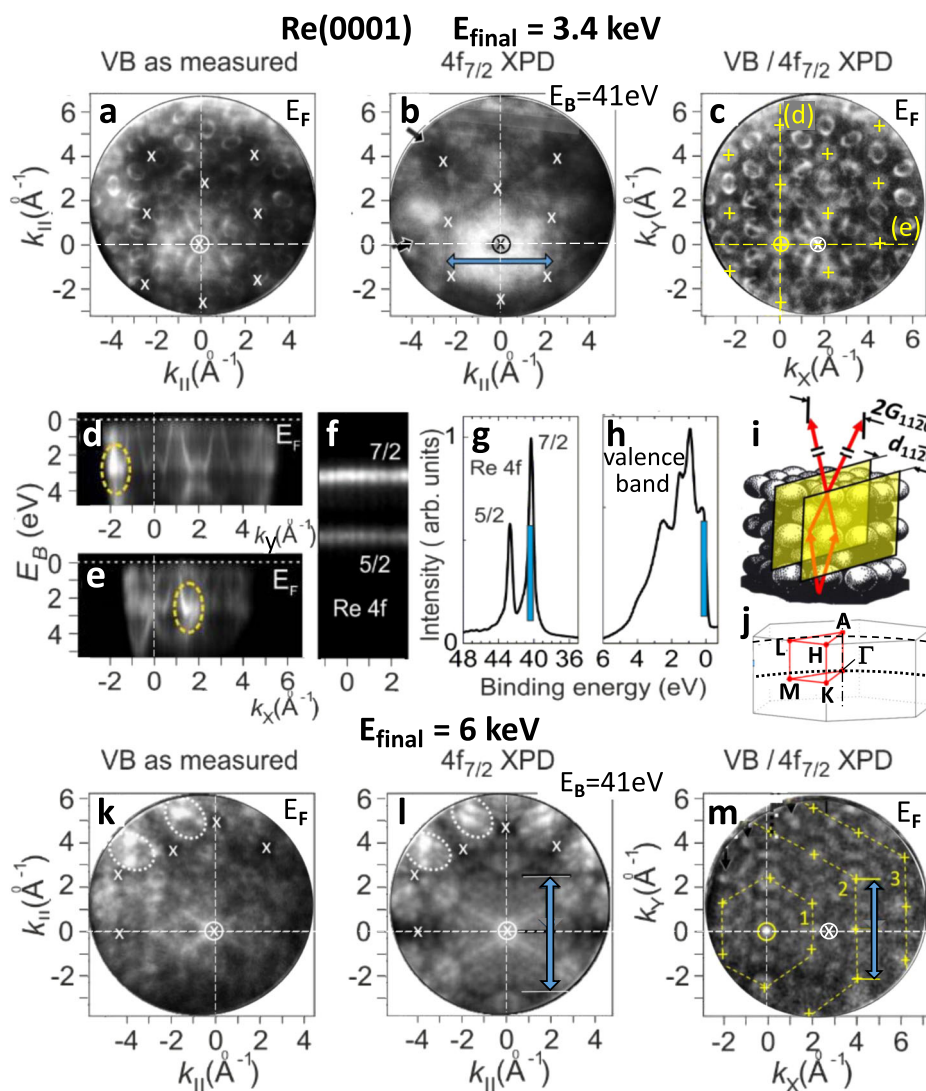
Fig. 8 Two types of photoelectron diffraction for Rhenium (0001) in the hard X-ray range. a As-measured valence-band (VB) (k_x, k_y) momentum pattern at the final-state energy $E_{final} = 3.4$ keV; crosses mark signatures of Kikuchi diffraction. **b** Re $4f_{7/2}$ core-level X-ray photoelectron diffraction (XPD) pattern taken at the same final-state energy and identical settings of the microscope. Crosses and ellipses mark the same features as in (**a**), the circled cross marks the centre of symmetry ([0001]-direction) and the double arrow marks the principal Kikuchi band (width $2|\boldsymbol{G}_{11-20}|$). **c** Ratio image of the valence-band pattern (VB) and the core-level diffractogram ($4f_{7/2}$ XPD) showing the valence-band structure with eliminated diffraction modulation. Pluses mark the centres of the Brillouin zones. **d**–**f** Binding energy E_B vs. momentum k_y, k_x sections of valence-band and $4f$ core-level signals. Dashed ellipses in (**d**, **e**) mark signatures of Laue-type diffraction. **g**, **h** Time-of-flight spectra for the Re $4f$ core level and valence band, respectively. The bars denote the energy regions integrated for momentum patterns (**a**) and (**b**). **i** Real-space model illustrating the origin of the principal Kikuchi band marked in (**b**) as double arrow. **j** Brillouin zone of the hexagonal-close-packed Re lattice. **k**–**m** Same as (**a**–**c**) but for 6.0 keV; crosses and dashed ellipses mark intensity-modulations by Kikuchi diffraction. Sections (**c**) and (**m**) run through different planes of the Brillouin zone (dashed and dotted lines in (**j**)). The lateral shifts of the valence-band pattern with respect to the [0001]-direction (difference between circled plusses and circled crosses in (**c**) and (**m**)) reflect the transfer of photon momentum $\boldsymbol{k}_{h\nu}$ to the valence-band photoelectrons.

patterns[26]. Figure 8b, l shows core-level diffractograms taken at the Re$4f_{7/2}$ signal (Fig. 8g). The photon energy was increased by 41 eV in order to shift the $4f_{7/2}$-signal to exactly the same final-state energy as the valence patterns; see spectra in Fig. 8g, h. All other settings of the microscope were kept fixed so that the k-scales stay identical, for later correction. At $E_{final} = 3.4$ keV the $4f_{7/2}$-XPD-pattern (Fig. 8b) shows a system of Kikuchi bands crossing under 120°, whose intersection region is visible as a bright hexagon centred at the [0001]-direction (circled cross). Position and size of the hexagon and dark areas in the XPD-pattern (Fig. 8b) agree with the structure imprinted on the valence-band-pattern in Fig. 8a.

The Re$4f_{7/2}$ XPD-pattern at $E_{final} = 6$ keV (Fig. 8l) exhibits a rich fine structure due to the shorter wavelength of the outgoing photoelectron and the larger inelastic mean-free path[36]. It also shows a system of Kikuchi bands, dark spots (marked by crosses) and bright regions (dashed ellipses). The centre of symmetry ($\boldsymbol{k} = 0$) shows a bright X-shaped feature (centre marked by a circled cross). All these characteristic features are visible in the measured valence-band momentum-image (Fig. 8k) as well. The model in Fig. 8i shows the lattice planes with distance d_{11-20}, leading to the outgoing rays forming the Kikuchi band (width $2\boldsymbol{G}_{11-20}$, see double arrows in Fig. 8b, l) in the k-microscope images. The centre of the images was shifted downwards in order to reach a larger radius in the upper part.

Following ref. [26], we eliminate the Kikuchi-modulation by multiplicative correction, yielding the pixel-by-pixel ratio of the as-measured VB-patterns (Fig. 8a, k) and the core-level diffractograms (Fig. 8b, l). In the ratio images (Fig. 8c, m) the diffraction modulation is largely eliminated and the true valence-band features are clearly visible. The two VB-patterns are different because at 6 keV the final-state sphere runs through the ΓMK-plane and at 3.4 keV close to the AHL-plane of the BZ (indicated by the dotted and dashed sectional planes in the BZ (Fig. 8j), respectively). The increased noise in Fig. 8m reflects the dramatic drop in cross section with increasing energy[26,37]. Close inspection reveals that Kikuchi diffraction acts on both the underlying background signal and the band features themselves. Remarkably, after the division regions of local intensity enhancement due to Laue-type diffraction are still present (marked by dashed ellipses in Fig. 8d, e).

The rigid shift of the entire VB k-distribution by the photon momentum is clearly visible in the difference between the centre of the Kikuchi patterns and the centre of the VB-patterns (marked by circled cross and circled plus in Fig. 8c, m, respectively). The Kikuchi patterns are symmetric to the crystallographic [0001]-direction at $k_\parallel = 0$ (b, l). The VB-patterns are defined on the k-scale of the band states (k_x, k_y), which refers to the centre (Γ-point) of the band structure (Fig. 8c, m). The transfer of $\boldsymbol{k}_{h\nu}$ shifts the origin of the (k_x, k_y)-scale (circled crosses) significantly away from the [0001]-direction (circled plusses). The curvature of the final-state sphere is clearly visible for such large k-fields. The intersection contour of the sphere with the periodic patterns of BZs runs through different k_z-values, as explained in Figs. 2a, b and 3c. In turn, the patterns in Fig. 8c, m are not strictly periodic because at the rim the k_z-values are smaller than in the centre. The photon polarization (p-polarized with electric vector tilted by 22° against the surface normal) causes asymmetries in the photoemission signal[31,38], which are still significant in the HAXPES range[39].

Discussion

We categorize the complex appearance of photoelectron diffraction into four different classes:

(i) Strong local intensity modulations (up to a factor of 5 in both directions) occur in the observed VB-patterns in all spectral ranges studied (15 eV–7 keV). The signatures of this mechanism are its strong confinement in (E_B, $\boldsymbol{k}$) parameter-space to intervals down to ∼200 meV and ∼0.03 Å^{-1} and its lack of symmetry and any visible systematics. A graphical model based on Umklapp processes on the final-state energy isosphere in k-space explains this type of XPD-modulation and its extremely rapid variation with energy and momentum. The missing symmetry in VB-XPD patterns reflects the transfer of photon momentum $\boldsymbol{k}_{h\nu}$ to the photoelectron, causing a rigid shift of the final-state sphere in k-space. We adopt the term Laue-type diffraction because VB-XPD deals with an energy band, similar to Laue-diffraction with an X-ray continuum[40]. This mechanism is "intrinsic" to the photoemission process, as the transfer of $\boldsymbol{k}_{h\nu}$ enters into the selection of the electron-wave-vector of the final state. It has first been introduced by Pendry et al.[32–35] in terms of the multiple-scattering final state ("time-reversed LEED-state"). The number of (E_B, $\boldsymbol{k}$)-regions in which the Laue condition is fulfilled increases with the number of BZs on the surface of the final-state energy isosphere. For $h\nu = 50$, 400, 1700 and 6000 eV, the numbers of BZs on the surface of the sphere are about 25, 170, 708 and 2488, respectively (taking the parameters for Mo from Fig. 2).

(ii) In the hard-X-ray range another mechanism, Kikuchi-diffraction, contributes to VB-XPD and becomes dominant at energies of several keV. The signatures of this effect are the long-range modulation of the VB-patterns by Kikuchi-bands and -lines and the fact that the modulation patterns reflect the full lattice symmetry. Different from the almost resonance-like Laue-type intensity modulation, the Kikuchi-modulation acts on the entire field of view and is "extrinsic" to the photoemission process, without participation of photon momentum.

(iii) The quasi-elastic background underlying the VB-patterns also shows a pronounced Kikuchi-type diffraction signature, characterized by a strong intensity increase with increasing final-state energy and temperature (Fig. 4 of ref. [26]). Although overlooked in the past, Kikuchi patterns in the background are not too surprising because such processes are also responsible for Kikuchi diffraction in scanning and transmission electron microscopy (SEM/TEM)[41–43] as discussed in detail by Wang[44]. Unlike SEM/TEM this background extends over a continuous energy band (typically more than 10 eV) in photoemission. Stochastic quasi-elastic scattering events of VB-photoelectrons (mostly thermally induced) cause a localization of the scattered electron. The coherence with the final-state-wave-field is lost, but the scattered wave is coherent again and experiences Kikuchi-diffraction at the lattice. Unlike Laue-type diffraction, this mechanism is "extrinsic" to the VB-photoemission process, since initial coherence is lost and $\boldsymbol{k}_{h\nu}$ is not involved. We found Kikuchi-modulations imprinted on the valence-band k-distributions and their background for all single-crystalline samples studied so far (W, Mo, Re, Ir, graphite, Si, GaAs, SrTiO$_3$, NbSe$_2$ and other transition-metal dichalcogenides).

(iv) The fourth category of XPD-signature, well-known from previous work[7,8,16,17], are the Kikuchi-patterns in core-level XPD, i.e. for monoenergetic energy distributions. Recording such patterns is most important for the correction algorithm described in ref. [26]. Comprehensive work in the field of electron microscopy (SEM and TEM) validated Kikuchi-diffraction as powerful tool for structural analysis[41–44].

The long-range-modulations on the VB-patterns need additional discussion. If a k-randomizing scattering event (like in the classical Kikuchi-process) were involved, the bands in the intensity-enhanced regions would not stay sharp. Apparently, the high-energy Bloch waves of the photoelectrons excited in the direct transition (with well-defined $\boldsymbol{k}_f$) experience Bragg-reflection at sets of lattice planes. This can be considered as "half" a Kikuchi-process (with missing initial scattering-step). This imprinted pattern has the same orientation, symmetry and metric as the classical Kikuchi-pattern imprinted on the background.

At this point we should have a look at the status of photoemission theories. The existing code for one-step photoemission calculations yields excellent agreement concerning band features observed with soft and hard X-rays[30]; its extension towards calculating VB-XPD by including photon-momentum and Laue-type Umklapp-processes is in progress. Measured CL-XPD patterns show excellent agreement with calculations using the Bloch-wave model between $h\nu = 2.8$–7.2 keV[45]. This opens a new avenue towards in situ structural analysis, simultaneously with VB-mapping. First results identifying two different sites of Te-atoms in a Si crystal, tracking an incommensurate−commensurate phase transition in TaS$_2$ or first time-resolved pump−probe experiments[46] give a glance on the potential of full-field imaging

CL-XPD. New approaches like adapting a Bloch-wave model to VB-XPD might help to understand the experimental observations and underlying processes more quantitatively. In generalization of the analysis of Fig. 6, the appearance of VB-XPD patterns could be predicted by feeding measured 4D spectral-density functions into a suitable computer program that would automatically find all possible diffraction conditions for a given photon energy.

We can consider the Laue- and Kikuchi-scenario as two diffraction-branches with fundamentally different characteristics: The Laue-type Umklapp-process is intrinsic and happens on the final-state energy isosphere, which is shifted in k-space by the photon momentum $\mathbf{k}_{h\nu}$. This diffraction branch can only be understood in a rigorous k-space treatment as presented in this paper. The Kikuchi signature, however, is extrinsic and governed by the orientation of the lattice planes and thus the modulation reflects the lattice symmetry. For Re at a temperature of 30 K and 3.4 keV the relative weight of the Kikuchi-branch is comparable to the Laue-branch, whereas at 6 keV the Kikuchi-branch is largely dominating. Since the Debye−Waller factor shows an exponential dependence on temperature[26], this ratio varies with dropping temperature in favour of the Laue-branch. The coexistence of several XPD-branches and the role of $\mathbf{k}_{h\nu}$ inducing the dramatic loss of symmetry go beyond Pendry's multiple-scattering final-state Ansatz and theoretical ab-initio treatment appears quite complex.

ARPES and k-microscopy in the X-ray range are rapidly gaining importance and excellent momentum and energy-resolution is achieved (e.g. ~60 meV at 6 keV[47]). However, the band maps observed at a given photon energy are strongly modulated by VB-XPD. The same is true for the linear and circular dichroism[48,49] and the spin-polarization texture[50]. If disregarded, this substantial influence of photoelectron diffraction on the observed band features including their dichroism and spin polarization can cause misinterpretations with respect to the spectral function and its spin-character.

Methods

Beamlines. The experiments have been carried out at two beamlines (P04 and P22) of the storage ring PETRA III at DESY in Hamburg and a VUV-beamline at BESSY II, Berlin. The hard X-ray measurements (Fig. 8) have been performed at beamline P22, which belongs to the beamlines with the highest brilliance worldwide in an energy range from 2.4 to 15 keV[51]. Conditions for the present experiments were 2×10^{13} photons/s at 4–6 keV in a spot of about $15 \times 20\ \mu m^2$. Using the Si(111) double-crystal monochromator the bandwidth varies from 350 meV in the 3 keV range to 500 meV at >6 keV. The Si(311) monochromator crystal yields a three times smaller bandwidth. At 5.3 keV we measured 450 and 155 meV for the Si(111) and (311) crystals, respectively, and at 5.977 keV an FWHM of 62 meV using the Si (333) crystal[47]. The resolving power for the (333)-crystal is >10^5.

For the soft X-ray measurements (Figs. 1–4, 6 and 7) we used beamline P04 of PETRA III[52] providing photons in the spectral range between 260 eV and 2 keV in a spot of <25 μm diameter. A photon bandwidth down to <30 meV at $h\nu = 1000$ eV provides an excellent energy resolution (4×10^4) in this range. The ToF drift energy was set to 30 eV, corresponding to a detector resolution of 40 meV, matching the photon bandwidth of the beamline in the respective energy range. This resulted in an overall instrumental energy resolution of ~50 meV. For P22 and P04 the 40-bunch mode of PETRA III provides a pulse period of 192 ns, well matched to the 5 MHz count-rate capability of the delay-line detector. Photon pulse widths are about 50 ps rms.

For the measurements in the VUV-range (Fig. 5) we used beamline U125/10 m NIM at BESSY II, Berlin, providing VUV photons in the range from 4 to 40 eV with a very high energy resolution of down to 0.5 meV. Photon flux in the single-bunch filling mode of the storage ring was up to 10^{12} photons/s in a spot of ~100 μm diameter. The single-bunch mode of BESSY II has a pulse rate of 1 MHz.

Instruments. All results except those in Fig. 8 have been obtained with the ToF momentum microscope described in ref. [29]. It combines the electron-optical imaging column[53] developed at the Max Planck Institute (Halle, Germany) with the ToF-recording technology of the Mainz group[54]. Figure 1a shows the recording geometry. The instrument exploits a general principle of optics: in the Fourier plane of the objective lens (backfocal plane) a momentum image (k-image) is

formed, which is a key feature for low-energy electron microscopy[55]. The subsequent zoom lenses project this k-image on the entrance plane of the image detector, in our setup a delay-line detector (DLD). For each electron the time of flight in the low-energy drift section of the microscope column is recorded, exploiting the time structure of the synchrotron radiation. ToF is converted into kinetic energy and calibrated at the Fermi edge yielding the binding energy E_B. A size-selectable field aperture in an intermediate real-space image plane facilitates the selection of well-defined source areas on the sample surface with diameters down to the μm-range. The imaged k-field of view has a linear momentum scale up to a diameter of ~7 Å^{-1}; for larger fields a significant field curvature appears (a well-known effect for wide-angle lenses). The deterministic part of the Coulomb interaction between the valence-band photoelectrons and the large number of secondary electrons was corrected employing the concept described in ref. [56].

For the investigation of the long-range Kikuchi-type diffraction patterns taken with hard X-rays from beamline P22 (results in Fig. 8), we used a ToF k-microscope with new optics, optimized for high initial kinetic energies up to >8 keV. Its novel type of objective lens can image large k-diameters up to ~22 Å^{-1}, comprising many Brillouin zones in parallel. The small photon footprint of ~$20 \times 30\ \mu m^2$ causes a large depth of focus of the k-images. In turn, large energy ranges are imaged with good focus in a single exposure. This instrument uses a DLD with 80 mm active area. The DLDs in both setups record count rates up to ~5 MHz at a spatial resolution of ~80 μm and a time resolution of 180 ps, yielding >1000 resolvable time slices at the given pulse period of 192 ns for the 40-bunch filling pattern of PETRA III. The measured energy resolution of the combination of DLD and imaging ToF-spectrometer (0.9 m long) at a drift energy of 10 eV is 17 meV, measured in a low-energy experiment using laser excitation.

Data recording. Valence-band 3D data arrays I(E_B, k_x, k_y) are recorded with acquisition times of typically 20 min at P04 and about 1 h at P22. The acquisition of core-level XPD patterns like in Fig. 8 is faster. The two momentum coordinates (k_x, k_y) are observed by full-field k-imaging and many binding energies E_B are taken simultaneously in a single exposure by recording the time coordinate (referenced to the photon pulse) of each individual counting event in the DLD. The sample is mounted on a He-cooled hexapod manipulator for precise six-axis adjustment. Most data have been recorded at sample temperatures around 30 K. The circularly polarized (at P04) or p-polarized photon beam (at P22) impinges at 22° with respect to the sample surface (Fig. 1a).

The high parallelization of data acquisition and the high brilliance of the beamlines compensate for the strong decrease of photoemission cross-section with increasing photon energy towards the hard X-ray range (Fig. 1 in ref. [26]). Count-rates exceeding 10^6 counts per second in an interval of ~15 eV are obtained in the valence range at all photon energies used. When recording core-level signals, a proper attenuation of the X-ray beam was necessary in order to avoid excessive count rates.

It is worthwhile to consider the momentum- and energy-resolution at high energies in the several-keV range. The band features appear sharp up to the maximum photon energy used (here 6 keV). With increasing binding energy the reduced lifetime of the photo-hole leads to a broadening of the band features. At E_F this broadening vanishes but at $E_B \sim 3$ eV the hole lifetime is 12.5 fs corresponding to 50 meV, being in the order of the overall instrumental resolution mentioned above. We do not observe a final-state broadening or smearing of k_z-resolution with increasing energy. This is most likely connected with the fact that the reciprocal space is a periodic pattern of BZs. Thus, except for the matrix elements that depend on photon energy, these patterns should be equivalent for direct transitions leading to low- or high-energy repeated BZs along k_z. The "transfer-width" argument is even in favour of high k_z-resolution at very high energies, because more and more unit cells contribute to the observed signal. Given the present experimental conditions we did not expect to observe recoil effects[24]; this issue is subject of ongoing experiments.

Determination of the Fermi surface and other energy isosurfaces. Isosurfaces like those in Figs. 2 and 3 are determined as follows (for an explicit example, see ref. [29]). The central task is mapping of the 4D spectral-density function $\rho(E_B;\mathbf{k})$ from which all energy isosurfaces, the electron velocity distribution at the Fermi surface and any other energy surface can be easily derived by simple algorithms. The lens optics is set to acquire 3D data arrays I($E_B;k_x,k_y$) with momentum slices of diameter ~20% larger than the BZ in a binding-energy range of ~6 eV width. A typical binning size for such measurements is 18 meV, yielding 330 momentum slices. Acquisition of such a 3D data array takes 10−20 min. The third momentum component k_z is varied by appropriate setting of the photon energy, as explained in Fig. 2a. For the isosurfaces of Mo and Re we took 20 equally spaced 3D arrays, covering the full selected BZ in detail. A sufficiently small step size for k_z accounts for the fact that for Mo and Re the isosurfaces are fragmented objects with several isolated electron and hole pockets (Fig. 2c–f). The k-slices of all 3D arrays are concatenated along the k_z-axis forming the 4D array, being the discretized experimental mapping of the so-called removal part of the spectral function $\rho(E_B;\mathbf{k})$, with intensities being weighted by the corresponding matrix elements. In the language of topology the Fermi surface is the boundary of the occupied part of ρ (termed support of ρ) as explained mathematically in ref. [29]. All other energy surfaces are defined analogously. The Fermi velocity or any other group velocity

$\mathbf{v}_E(\mathbf{k})$ is oriented perpendicular to the corresponding isosurface and is given by the gradient of $E(\mathbf{k})$ in k-space at the energy of interest.

Sample preparation. The refractory metal crystals W, Mo, Re, Ir were cleaned by repeated cycles of heating in oxygen followed by desorption of the surface oxide by a flash at high temperature. The base pressure during the experiment was 4×10^{-10} mbar. Prior to the soft X-ray measurements the surface quality was verified by LEED. Layered samples like graphite and the transition-metal dichalcogenides were cleaved in UHV prior to transfer to the microscope chamber. No traces of impurities, as judged, for example, by C 1s and O 1s spectra, were present in the spectra. Since it is operated in the shielding hutch at P22 all lens voltages, the data acquisition system and all mechanical adjustment parameters (hexapod, frame position, apertures of the microscope) are fully remote controlled.

Data availability

The data that support the findings of this study are available from the corresponding author upon reasonable request.

References

1. Fadley, C. S. & Nemsak, S. Some future perspectives in soft- and hard-X-ray photoemission. *J. Electron. Spectrosc. Relat. Phenom.* **199**, 408–423 (2014).
2. Strocov, V. N. et al. k-resolved electronic structure of buried heterostructure and impurity systems by soft-X-ray ARPES. *J. Electron Spectrosc. Relat. Phenom.* **236**, 1–8 (2019)
3. Woicik, J. C. (ed.) *Hard X-ray Photoelectron Spectroscopy (HAXPES)*, Springer Series in Surface Sciences, Vol. 59 (Springer International Publishing, Switzerland, 2016).
4. Fadley, C. S., Van Hove, M. A., Hussain, Z. & Kaduwela, A. P. Photoelectron diffraction: new dimensions in space, time, and spin. *J. Electron. Spectrosc. Relat. Phenom.* **75**, 273 (1995) and references therein.
5. Woodruff, D. P. & Bradshaw, A. M. Adsorbate structure determination on surfaces using photoelectron diffraction. *Rep. Prog. Phys.* **57**, 1029 (1994).
6. Westphal, C. The study of the local atomic structure by means of X-ray photoelectron diffraction. *Surf. Sci. Rep.* **50**, 1–106 (2003).
7. Winkelmann, A., Fadley, C. S. & Garcia de Abajo, F. J. High-energy photoelectron diffraction: model calculations and future possibilities. *N. J. Phys.* **10**, 113002 (2008).
8. Fadley, C. S. X-ray photoelectron spectroscopy: progress and perspectives. *J. Electron. Spectrosc. Relat. Phenom.* **178–179**, 2 (2010).
9. Woodruff, D. P. Surface structural information from photoelectron diffraction. *J. Electron. Spectrosc. Relat. Phenom.* **178–179**, 186 (2010).
10. Osterwalder, J. in *Handbook on Surface and Interface Science* Vol. 1 (ed. Wandelt, K.), 151−214 (Wiley-VCH, Weinheim, 2011).
11. Kobayashi, K., Kobata, M., Masaaki, I. & Iwai, H. Development of a laboratory system hard X-ray photoelectron spectroscopy and its applications. *J. Electron. Spectrosc. Relat. Phenom.* **190**, 210–221 (2013).
12. Woodruff, D. P. & Bradshaw, A. M. J. Structure determination of molecular adsorbates using photoelectron diffraction. in (ed. Eberhardt, W.) Applications of Synchrotron Radiation, Springer 1995, p. 127–169
13. Siegbahn, K., Gelius, U., Siegbahn, H. & Olson, E. Angular distribution of electrons in ESCA spectra from a single crystal. *Phys. Scripta* **1**, 272 (1970).
14. Fadley, C. S. & Bergstrom, S. A. L. Angular distributions of photoelectrons from a metal single crystal. *Phys. Lett.* **35A**, 375 (1971).
15. von Laue, M. *Materiewellen und ihre Interferenzen* (Akademische Verlagsgesellschaft Geest & Portig, Leipzig, 1948).
16. Goldberg, S. M., Baird, R. J., Kono, S., Hall, N. F. T. & Fadley, C. S. Explanation of XPS core-level angular distributions for single-crystal copper in terms of two-beam Kikuchi-band theory. *J. Electron. Spectrosc. Relat. Phenom.* **21**, 1 (1980).
17. Trehan, R., Fadley, C. S. & Osterwalder, J. Single-scattering cluster description of substrate X-ray photoelectron diffraction and its relationship to Kikuchi bands. *J. Electron. Spectrosc. Relat. Phenom.* **42**, 187 (1987).
18. Garcia de Abajo, F. J., Van Hove, M. A. & Fadley, C. S. Multiple scattering of electrons in solids and molecules: a cluster-model approach. *Phys. Rev. B* **63**, 075404 (2001).
19. Osterwalder, J., Greber, T., Hüfner, S. & Schlapbach, L. X-ray photoelectron diffraction from a free-electron-metal valence band: evidence for hole-state localization. *Phys. Rev. Lett.* **64**, 2683 (1990).
20. Herman, G. S., Tran, T. T., Higashiyama, K. & Fadley, C. S. Valence Photoelectron diffraction and direct transition effects. *Phys. Rev. Lett.* **68**, 1204 (1992).
21. Osterwalder, J., Greber, T., Aebi, P., Fasel, R. & Schlapbach, L. Final-state scattering in angle-resolved ultraviolet photoemission from copper. *Phys. Rev. B* **53**, 10209 (1996).
22. Sondergaard, Ch et al. Symmetry-resolved density of states from valence band photoelectron diffraction. *Phys. Rev. B* **64**, 245110 (2001).
23. Krüger, P., Da Pieve, F. & Osterwalder, J. Real-space multiple scattering method for angle-resolved photoemission and valence-band photoelectron diffraction and its application to Cu(111). *Phys. Rev. B* **83**, 115437 (2011).
24. Kayanuma, Y. in *Hard X-ray Photoelectron Spectroscopy (HAXPES)*, Springer Series in Surface Sciences Ch. 8, Vol. 59 (Springer International Publishing, Switzerland, 2016).
25. Braun, J., Minár, J. & Ebert, H. Correlation, temperature and disorder: recent developments in the one-step description of angle-resolved photoemission. *Phys. Rep.* **740**, 1–34 (2018) and references therein.
26. Babenkov, S. et al. High-accuracy bulk electronic structure mapping: momentum-resolved hard X-ray photoelectron spectroscopy with eliminated diffraction effects. *Comms. Phys.* **2**, 107 (2019).
27. Hüfner, S. *Photoelectron Spectroscopy—Principles and Applications* (Springer, Berlin, 2003).
28. Reinert, F. & Hüfner, S. Photoemission spectroscopy—from early days to recent applications. *N. J. Phys.* **7**, 97 (2005).
29. Medjanik, K. et al. Direct 3D mapping of the Fermi surface and Fermi velocity. *Nat. Mat.* **16**, 615 (2017).
30. Gray, A. X. et al. Probing bulk electronic structure with hard X-ray angle-resolved photoemission. *Nat. Mat.* **10**, 759 (2011).
31. Plummer, E. W. & Eberhardt, W. in *Advance in Chemical Physics* Vol. XLIX (eds Prigogine, I. & Rice, S. A.), 533−656 (John Wiley, 1982).
32. Pendry, J. B. Theory of photoemission. *Surf. Sci.* **57**, 679–705 (1976).
33. Pendry, J. B. & Hopkinson, J. F. L. Theory of photoemission. *J. Phys. Colloques* **39**, C4-142–C4-148 (1978).
34. Hopkinson, J. F. L., Pendry, J. B. & Titterington, D. J. Calculation of photoemission spectra for surfaces of solids. *Comput. Phys. Commun.* **19**, 69–92 (1980).
35. Pendry, J. B. *Low Energy Electron Diffraction* (Academic Press, London, 1974).
36. Tanuma, S. et al. Calculations of electron inelastic mean free paths. IX. Data for 41 elemental solids over the 50 eV to 30 keV range. *Surf. Interface Anal.* **43**, 689–713 (2011).
37. Trzhaskovskaya, M. B. et al. Dirac-Fock photoionization parameters for HAXPES applications. *Data Nucl. Data Tables* **119**, 99–174 (2018).
38. Goldberg, S. M., Fadley, C. S. & Kono, S. Photoionization cross-sections for atomic orbitals with random and fixed spatial orientation. *J. Electron. Spectrosc. Relat. Phenom.* **21**, 285–363 (1981).
39. Suga, S. & Sekiyama, A. *Photoelectron Spectroscopy—Surface and Bulk Electronic Structures*, Springer Series in Optical Sciences Ch. 8.8 (Springer 2014).
40. Kittel, C. *Introduction to Solid State Physics* (John Wiley & Sons, New York, 1976).
41. Kikuchi, S. Diffraction of cathode rays by mica. *Proc. Imp. Acad.* **4**, 354–356 (1928).
42. Reimer, L. *Scanning Electron Microscopy—Physics of Image Formation and Microanalysis* (Springer, Berlin, New York, 1998).
43. Williams, D. B. & Carter, C. B. *Transmission Electron Microscopy* Ch. 11 (Springer, Boston, 2009).
44. Wang, Z. L. Thermal diffuse scattering in sub-angstrom quantitative electron microscopy—phenomenon, effects and approaches. *Micron* **34**, 141–155 (2003).
45. Fedchenko, O. et al. High-resolution hard-X-ray photoelectron diffraction in a momentum microscope—the model case of graphite. *N. J. Phys.* **21**, 113031 (2019).
46. Kutnyakhov, D., et al., Momentum and time-resolved photoemission studies using time-of-flight momentum microscopy at a free electron laser. *Rev. Sci. Instrum.* **91**, 013109 (2020).
47. Medjanik, K. et al. Progress in HAXPES performance combining full-field k-imaging with time-of-flight recording. *J. Synchr. Radiat.* **26**, 1996 (2019).
48. Chernov, S. V. et al. Anomalous d-like surface resonances on Mo(110) analyzed by time-of-flight momentum microscopy. *Ultramicroscopy* **159**, 463 (2015).
49. Fedchenko, O. et al. 4D texture of circular dichroism in soft-x-ray photoemission from tungsten. *N. J. Phys.* **21**, 013017 (2019).
50. Vasilyev, D. et al. Relation between spin–orbit induced spin polarization, Fano-effect and circular dichroism in soft x-ray photoemission. *J. Phys. Cond. Matter* **32**, 135501 (2020).
51. Schlueter, C. et al. New HAXPES applications at PETRA III. *AIP Conf. Proc.* **2054**, 040010 (2019).
52. Viefhaus, J. et al. The Variable Polarization XUV Beamline P04 at PETRA III: optics, mechanics and their performance. *Nucl. Instrum. Methods* **710**, 151–154 (2013).
53. Tusche, C., Krasyuk, A. & Kirschner, J. Spin resolved band structure imaging with a high resolution momentum microscope. *Ultramicroscopy* **159**, 520–529 (2015).

54. Oelsner, A. et al. Microspectroscopy and imaging using a delayline-detector in time-of-flight photoemission microscopy. *Rev. Sci. Instrum.* **72**, 3968–3974 (2001).

55. Bauer, E. LEEM and UHV-PEEM: a retrospective. *Ultramicroscopy* **119**, 18–23 (2012).

56. Schönhense, B. et al. Multidimensional photoemission spectroscopy—the space-charge limit. *N. J. Phys.* **20**, 033004 (2018).

Author contributions

G.S. and H.-J.E. wrote the paper and coordinated the project. K.M., S.B., D.V., M.E., O.F., S.C. and B.S. set up and carried out the experiment and prepared the samples. All authors discussed the results and contributed to the writing of the manuscript.

Competing interests

The authors declare no competing interests.

Additional information

Supplementary information is available for this paper at https://doi.org/10.1038/s42005-020-0311-9.

Correspondence and requests for materials should be addressed to G.S.

Reprints and permission information is available at http://www.nature.com/reprints

Publisher's note Springer Nature remains neutral with regard to jurisdictional claims in published maps and institutional affiliations.